Double dating sedimentary sequences using new applications of in-situ laser ablation analysis

Darwinaji Subarkah [a,*], Angus L. Nixon [a], Sarah E. Gilbert [b], Alan S. Collins [a,c], Morgan L. Blades [a], Alexander Simpson [d], Jarred C. Lloyd [a], Georgina M. Virgo [a], Juraj Farkaš [a,c]

[a] School of Physics, Chemistry, and Earth Science, University of Adelaide, Adelaide, SA 5005, Australia
[b] Adelaide Microscopy, Adelaide, SA 5005, Australia
[c] MinEx CRC, Australian Resources Research Centre, Perth, WA 6151, Australia
[d] British Geological Survey, Nottingham NG12 5GG, United Kingdom

ARTICLE INFO

ABSTRACT

Sedimentary rocks can provide important insights regarding the evolution of Earth's surface environments through deep time. Such sequences are pervasive through the geological record and currently cover >70% of the planet's surface. They are also a key repository for energy and mineral resources. However, absolute chronology of sedimentary rocks can be difficult to constrain using conventional methods due to their typically low abundances of radiogenic elements. Establishing chronology is particularly challenging for Precambrian sedimentary rocks, where the lack of a diverse fossil record makes biostratigraphic correlations ambiguous. In this study, we use shale and carbonate samples from the Proterozoic greater McArthur Basin in northern Australia as a case study to demonstrate two emerging in-situ laser-based methods that have the potential to quickly and accurately resolve the minimum depositional age of a sedimentary package. The first method provides a tool to constrain the formation of authigenic clay minerals in shales using in-situ laser ablation Rb—Sr geochronology. The second method demonstrates an approach for dating carbonate sedimentation using U—Pb geochronology via a laser isotopic mapping approach. Laser rasters are compiled into isotopic maps, and this spatial and geochemical information is used to target representative subdomains within the sample. Detrital or altered regions can be avoided by monitoring chemical signatures and pixels, and to the most authigenic domains are then subdivided that give the best spread of data on an isochron. Both approaches provide the key advantage of preserving, and through the mapping approach further resolving, sample petrographic context, which together with complementary geochemical data can be triaged to yield a more appropriate age and interpretation.

1. Introduction

Sedimentary rocks are important repositories of evidence to help reconstruct past biogeochemical cycles on the Earth's surface (Lyons et al., 2021). Their geochemical signatures have been used to track the oxygenation of ancient oceans and atmospheres (Cox et al., 2022; Holland, 2006; Lyons et al., 2014), evolution and productivity of early life (Mukherjee and Large, 2020), and the formation and subsequent break-up of supercontinents (Chen et al., 2022). Furthermore, sedimentary sequences host significant and vital economic resources. These successions are commonly the source and/or trap for hydrocarbons as well as other naturally-occurring gases such as helium and hydrogen (Hunt, 1995; Levorsen and Berry, 1967). Additionally, they can also be prospective for mineral systems; hosting base-metals and critical minerals such as Cu, Pb, U, and Zn (Lyons et al., 2006) as well as rare earth element (REE) deposits (Spandler et al., 2020).

Despite their importance, establishing absolute geochronology of sedimentary rock formations has often proven challenging. This is especially true for successions in the Precambrian, where biostratigraphy is impractical due to the lack of biodiversity in the fossil record (Gradstein, 2012). Dating interbedded tuffaceous layers still remains the most precise and accurate method to obtain the depositional age of a sedimentary unit due to the presence of rapidly crystalized minerals analysed for traditional high-precision geochronology (McDougall, 2013; Page et al., 2000), however, such tuffs are not ubiquitous in all basin systems or packages. Consequently, demand for alternative

methods for directly dating sedimentary units has become paramount, with a number of emergent novel techniques providing options to address these shortcomings.

The first method applied in this study is the in-situ Rb—Sr dating of authigenic clays in shales. In-situ Rb—Sr geochronology has recently been made possible due to advancements in the Laser Ablation Inductively-Coupled Plasma Tandem Mass-Spectrometry (LA-ICP-MS/MS) technique (Zack and Hogmalm, 2016). Isobaric ^{87}Rb and ^{87}Sr isotopes can be separated online by introducing an oxide gas into a reaction cell which is located between two quadrupoles in an ICP-MS/MS set-up (Hogmalm et al., 2017; Redaa et al., 2021; Zack and Hogmalm, 2016). This approach removes the need for whole-rock digestion and column chemistry to separate the isobaric interference between the two isotopes (Nebel, 2014). The use of quadrupole MS/MS instruments also allows the user to benefit from quicker and easier sample preparation, high spatial control on their sample, faster analysis time, and the simultaneous collection of other elemental data to help interpret their geochronological results with this novel technique (Hogmalm et al., 2017; Redaa et al., 2021; Zack and Hogmalm, 2016). This method has recently been used to date K-rich (and therefore Rb-bearing) minerals in shales and other sedimentary rocks to directly constrain their depositional history (Drake et al., 2023; Lan et al., 2024; Laureijs et al., 2021; Lloyd et al., 2023; Rafiei, 2023; Rafiei et al., 2023; Redaa et al., 2023; Rösel et al., 2023; Scheiblhofer et al., 2022; Subarkah et al., 2022; Subarkah et al., 2022; Subarkah et al., 2023; Wu et al., 2023).

Another, complementary, technique applicable for establishing absolute sediment chronology is the U—Pb dating of calcite and other carbonate minerals, which commonly precipitate from the water-column and incorporate uranium during their formation (Jahn et al., 1990; Rasbury and Cole, 2009). Similar to the conventional Rb—Sr method, the traditional technique requires whole-rock chemical dissolution to prepare for analyses, followed by isotopic measurements by either Thermal Ionisation Mass Spectrometry (TIMS) or a solution ICP-MS (Jahn et al., 1990; Rasbury and Cole, 2009). Li et al. (2014) showed the potential for this method to be performed in-situ using an LA-ICP-MS. The popularity of carbonate U—Pb geochronology via microbeam analysis has expanded accordingly, as carbonates are present in a wide-array of geological settings (Elisha et al., 2021; Roberts et al., 2020; Roberts and Holdsworth, 2022). However, there are several factors that can still inhibit the universal application of this method. More so than other phases, carbonate minerals can readily experience local open system behaviour as they are sensitive to diagenetic, hydrothermal, and metamorphic processes (Bau and Dulski, 1996; Rimstidt et al., 1998; Sippel and Glover, 1964). These reactions can induce geochemical heterogeneity or form multiple generations of carbonate minerals, which may lead to unreliable or mixed-age results (Roberts et al., 2021). Furthermore, high incorporation of common Pb and/or low U concentrations within the sample can reduce age precision (Rasbury and Cole, 2009; Roberts et al., 2020). As such, targeting one carbonate generation with sufficient U and radiogenic Pb while avoiding detrital or alteration components within a sample can prove challenging.

In order to help resolve these limitations, Drost et al. (2018) demonstrated an image mapping approach to U—Pb LA-ICP-MS carbonate dating. The 2D maps generated combine geochemical, geochronological, and petrographic information together in order to help spatially resolve regions of interest within a sample. Regions within the maps can be filtered by geochemical criteria to screen for non-carbonate or non-cogenetic phases and aid in selecting the most pristine carbonate with enough U for a successful analysis (Chew et al., 2021; Drost et al., 2018). Pixels within these regions can then be pooled and subdivided into individual analytical points that provide the best spread along an isochron to yield precise geochronological results (Chew et al., 2021; Drost et al., 2018; Hoareau et al., 2021). This technique has been shown to reliably date carbonates with complex histories in other geological settings by systematically isolating a particular, dateable, cogenetic phase (Chew et al., 2021; Drost et al., 2018; Hestnes et al.,

2023; Kim et al., 2023; Monchal et al., 2023).

This study demonstrates the complementary application of both emerging Rb—Sr and U—Pb techniques to double date sedimentary successions and directly constrain their depositional history, targeting shale and carbonate lithologies within complex sedimentary sequences to maximise stratigraphic coverage. Samples from the Amos Formation and the Balbirini Dolostone from the Proterozoic greater McArthur Basin in northern Australia were used as a case study (Fig. 1). The in-situ Rb—Sr dating method was applied to K-rich, clay bearing, shale samples whilst the U—Pb mapping approach was used to analyse carbonate beds within the same measured section to independently verify each respective isotopic system.

2. Geological background

The greater McArthur Basin is a Palaeo-Mesoproterozoic intracontinental basin system overlying the North Australian Craton. It encompasses rocks from the McArthur Basin sensu stricto (Fig. 1), the Birrindudu Basin, and the Tomkinson Province (Close, 2014). These individual basins have been interpreted as laterally continuous in the subsurface based on geophysical, geochemical, geochronological, and sedimentological correlations (Ahmad and Munson, 2013; Close, 2014; Collins, 2019; Cox et al., 2022; Page et al., 2000). The units of the greater McArthur Basin are subdivided into five basin-scale packages based on their age, lithostratigraphy, igneous composition, and basin-fill geochemistry (Ahmad and Munson, 2013; Close, 2014). Samples from the Amos Formation and the Balbirini Dolostone (Fig. 1) from the Glyde Package are the focus of this study (Ahmad and Munson, 2013; Close, 2014; Jackson et al., 1987; Munson, 2019).

The lower section of the Amos Formation consists of clastic red-beds interpreted to have been deposited under terrestrial conditions (Pietsch, 1991). The unit conformably transitions into stromatolitic dolostone and dolarenite interbedded with siltstone and intraclast-rich conglomerate up stratigraphy (Jackson et al., 1987; Munson, 2019; Pietsch, 1991). The upper section of the Amos Formation is interpreted to have been deposited in a shallow-marine or peritidal environment (Jackson et al., 1987; Pietsch, 1991). Previous Sensitive High-Resolution Ion Microprobe (SHRIMP) U—Pb geochronology of zircons from tuff beds in the formation gave an age of 1614 ± 4 Ma (Page et al., 2000).

The Balbirini Dolostone type section was divided into three informal units by Jackson et al. (1987). The stratigraphically lower 'evaporitic unit' consists of red beds interbedded with fine-grained sandstone, pink tuffaceous beds, and shale with minor dolostone components (Jackson et al., 1987; Kositcin and Munson, 2020; Munson, 2019). Evaporitic indicators observed in this section include halite casts, gypsum pseudomorphs, as well as anhydrite casts (Kositcin and Munson, 2020). The formation transitions into the 'stromatolitic unit' in its medial section, characterised by cyclic dolostones, extensive stromatolitic markers, and algal-laminated dolomudstone (Jackson et al., 1987; Kositcin and Munson, 2020). The top 'recrystallised unit' comprises of thickly bedded stromatolite and silicified dolarenite with ripple structures and cross-bedding (Jackson et al., 1987; Kositcin and Munson, 2020; Munson, 2019). The red beds in this formation were interpreted to represent a continental sabkha and the carbonate successions were possibly deposited in a lacustrine or shallow-marine environment (Jackson et al., 1987; Pietsch, 1991). Samples previously analysed for geochronological constraints on the Balbirini Dolostone were sourced from this type section, which is also the same locality in which tuff beds from the Amos Formation were sampled. Note that the shale and carbonate samples of the Balbirini Dolostone in this study were also collected from the same measured section. SHRIMP U—Pb geochronology of zircons from two tuff beds in the lower 'evaporitic unit' of the formation gave ages of 1613 ± 4 Ma and 1609 ± 3 Ma (Page et al., 2000). Sandstone samples from the basal 'evaporitic unit' and the medial 'stromatolitic unit' were also analysed for SHRIMP U—Pb detrital zircon geochronology and yielded maximum depositional ages of 1625 ± 14 Ma and 1607 ± 6 Ma,
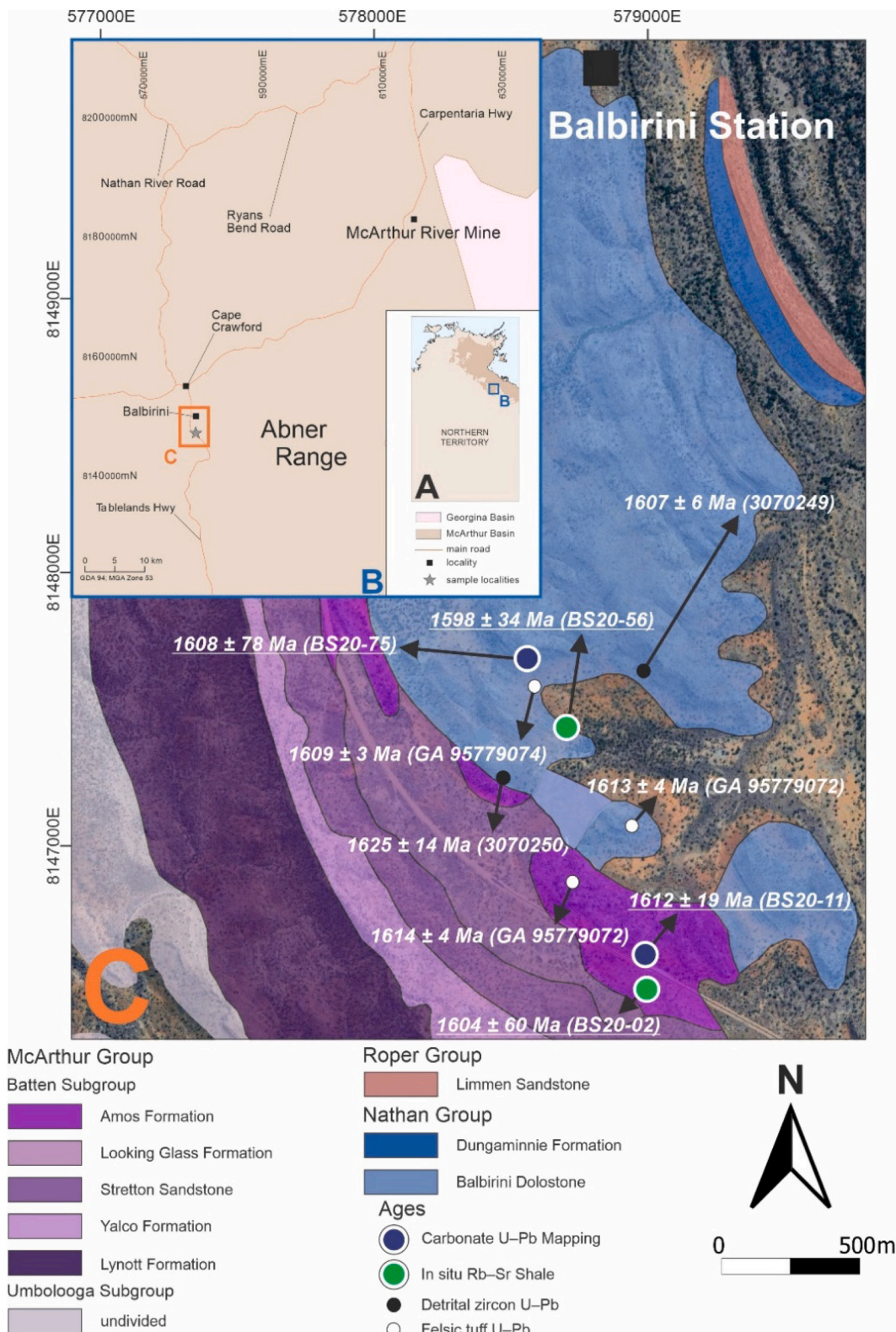
Fig. 1. A. Location of McArthur Basin in Northern Territory, Australia following Ahmad and Munson (2013). **1B—C.** Localities of samples in this study along with previous geochronological constraints for the Amos Formation and the Balbirini Dolostone (Kositcin and Munson, 2020; Page et al., 2000).

respectively (Kositcin and Munson, 2020).

3. Methods

Shale and carbonate samples from the Amos Formation and the

Balbirini Dolostone used in this study were collected from their respective type-sections (Fig. 1). A brief summary of samples analysed in this study can be found in Table 1.

Table 1

Summary of samples used in this study. Eastings and northings correspond to the Map Grid of Australia 1994 (MGA94) Zone 53.

Sample No.	Unit Name	Rock Type	Easting (mE)	Northing (mN)
BS20–02	Amos Formation	Very fine-grained siltstone	578,990	8,146,605
BS20–11	Amos Formation	Massive dolostone	578,995	8,146,475
BS20–56	Balbirini Dolostone	Fine-grained siltstone	578,712	8,147,448
BS20–75	Balbirini Dolostone	Massive dolostone	578,547	8,147,676

3.1. Backscatter electron and mineral mapping

Samples from the Amos Formation and the Balbirini Dolostone were first imaged for mineralogical and petrographic information prior to laser ablation analysis (Fig. 2–5). Maps were produced from backscatter electron (BSE) imaging and Mineral Liberation Analysis (MLA) using a Hitachi SU3800 automated mineralogy scanning electron microscope (SEM) at Adelaide Microscopy following Subarkah et al. (2022). BSE image tiles were collected at a working distance of 10 mm and 15 kV acceleration voltage. MLA maps were completed by stitching together consecutive linear raster analysis. MLA maps of carbonate samples were collected at 2.5 μm/pixel while shale samples were mapped at a higher spatial resolution of 0.8 μm/pixel to better define the mineralogy of the finer-grained sediments. Data were processed using the BRUKER AMICS Automated Mineralogy System processing software for SEM.

3.2. In-situ Rb—Sr geochronology by LA-ICP-MS/MS

In-situ Rb—Sr geochronology and trace element analysis of samples in this study was conducted at Adelaide Microscopy using an Agilent 8900× ICP-MS/MS coupled to a RESOlution ArF Excimer 193 nm laser ablation system following Redaa et al. (2021) and Redaa et al. (2023). The laser conditions and analytical parameters used in this study are summarised in Table 2. Laser ablation data were processed using LADR software package version 1.1.07, with Mica-Mg as the primary reference material for the $^{87}Rb/^{87}Sr$ ratios (Hogmalm et al., 2017) and NIST610 as the primary reference material for $^{86}Sr/^{87}Sr$ ratios and elemental data (Hogmalm et al., 2017; Jochum et al., 2011). The granulated texture of the nano-powder Mica-Mg have been interpreted to make an appropriate matrix analogue for fine-grained clays in sedimentary rocks (Subarkah et al., 2022). This is discussed in Subarkah et al. (2022), where Mica-Mg, a powdered illite-separate sample, and fine-grained clays in shales were shown to have similar laser-ablation pit profiles and down-hole fractionation patterns. These findings indicate that these materials have comparable ablation characteristics and no further correction factors were needed to calculate an accurate age result. This is also evidenced by other studies which have yielded accurate age data from in-situ Rb—Sr geochronology of clay minerals while using Mica-Mg as a primary standard without any additional secondary matrix corrections (Lan et al., 2024; Laureijs et al., 2021; Lloyd et al., 2023; Rafiei, 2023; Rafiei et al., 2023; Rösel et al., 2023; Scheiblhofer et al., 2022; Subarkah et al., 2022; Subarkah et al., 2023; Wu et al., 2023).

The phlogopite MDC is the natural flake source mineral of Mica-Mg (Hogmalm et al., 2017; Redaa et al., 2021; Redaa et al., 2023) and was used as a secondary standard along with the glauconite GL-O (Derkowski et al., 2009; Redaa et al., 2023). Trace element signatures of Zr, Si, and Ti were monitored to assess the detrital component of each analysis during data reduction (Subarkah et al., 2022). Isotopic signals that were not stable during an ablation period were removed to ensure spot homogeneity of each analytical point (Redaa et al., 2021; Subarkah et al., 2022). Ages were calculated using inverse isochrons (Nebel, 2014; Nicolaysen, 1961) following Li and Vermeesch (2021) using the IsoplotR processing package (Vermeesch, 2018). Reported uncertainties are provided at the 2SE level and includes propagated reference material and decay constant uncertainties.

3.3. U–Pb and trace element mapping by LA-ICP-MS

Laser mapping of samples in this study were performed at Adelaide Microscopy using an Agilent 8900× ICP-MS/MS coupled to a RESOlution ArF Excimer 193 nm laser ablation system following Drost et al. (2018). A 4 mm outer diameter nylon tubing was used to connect the ablation chamber and the ICP-MS instrument. The laser conditions and

BS20-02 Amos Formation
- Albite
- Pyrite
- Biotite
- Calcite
- Glauconite
- Hematite
- Illite
- Muscovite
- Quartz
- Pores
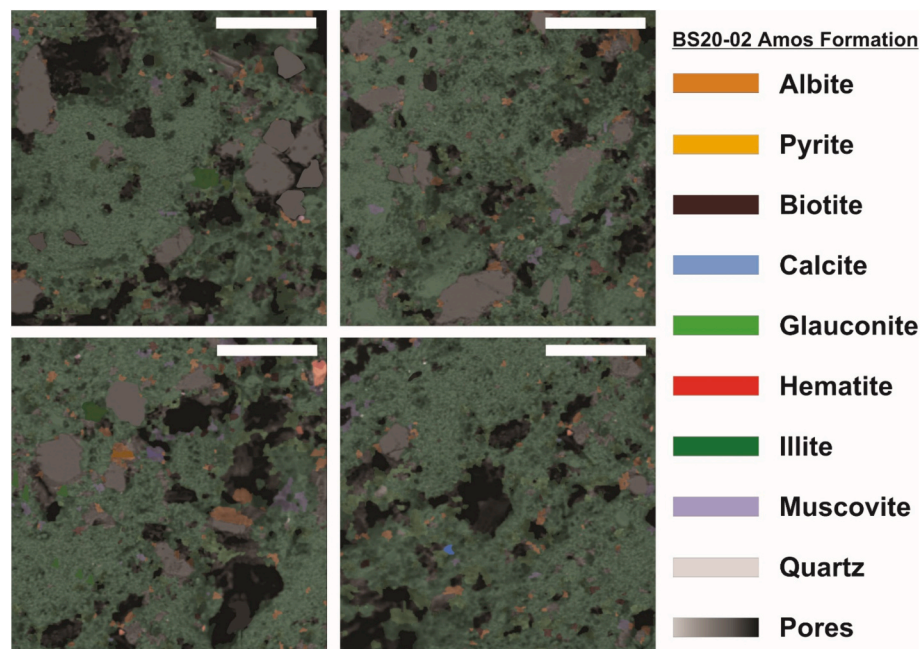
Fig. 2. Mineralogy and petrography of shale sample BS20–02 from the Amos Formation. Note that illite here form a fine-grained matrix cementing larger detrital minerals. White bar = 100 μm.
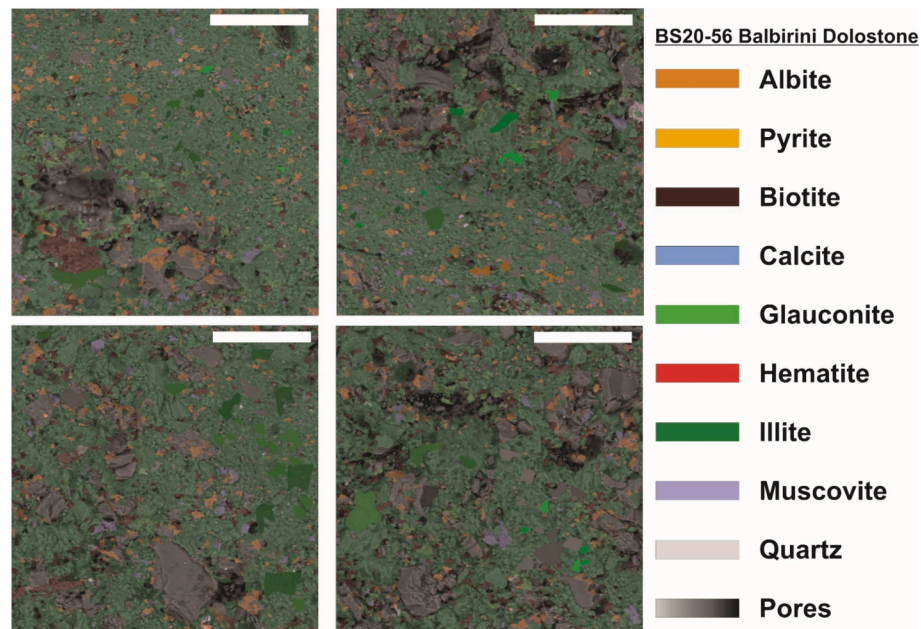
Fig. 3. Mineralogy and petrography of shale sample BS20–56 from the Balbirini Dolostone. Illite morphology here looks mottled and can be observed nestling detrital grains. White bar = 100 μm.

analytical parameters used for the mapping analysis are summarised in Table 3. Successive raster scans were programmed with no overlaps or gaps between each line to produce a coherent region of analysis. Each unknown sample is bracketed by two analyses of NIST612 (Jochum et al., 2011), two analyses of WC-1 (Roberts et al., 2017), and two analyses of Mexican Tank (Hill et al., 2016). In addition, eleven raster analyses of Duff Brown Tank were also analysed as a secondary check of a known age (Hill et al., 2016). Each Reference Material raster analyses consist of 30 s ablation time. Data were processed following Drost et al. (2018) using Iolite 4's Trace Element Data Reduction Scheme (DRS) and the U—Pb Geochronology DRS (Paton et al., 2011; Petrus et al., 2017). A stoichiometric Ca value for dolomite were used to calculate quantitative trace element data after samples were screened for detrital and secondary mineral phases. Laser maps are smoothed using Iolite 4's built in box smoothing, Gaussian 2D, and median filters. Regions enriched in proxies for detritus (e.g. Al, Si, Rb, Zr, and Th) were discounted from further investigations. In addition, proxies for post-depositional alteration in carbonates (e.g. Mn/Sr ratios, Fe, and Y) were also avoided (Bau and Dulski, 1996; Brand and Veizer, 1980; Rimstidt et al., 1998; Sippel and Glover, 1964). The cut-off criteria (processed in Counts Per Second) used and the geochemical raster maps for the samples in this study are reported in the Supplementary Material.

The pixels which pass the screening criteria demonstrate characteristics of a single, unaltered carbonate phase; with similar geochemistry and petrographic features. While this cannot be completely verified using a combination of spectral phase mapping (e.g. MLA) and element and isotope mapping via LA-ICP-MS, such criteria provide significantly more robust tests than may be commonly applied to single-spot dating and interpretation. Hence, pixels which passed these criteria have been interpreted as components of an unaltered, non-detrital carbonate of monogenetic affinity. These regions nonetheless exhibit heterogeneity in $^{238}U/^{208}Pb$ that are harnessed to create an isochron. These pixels were then pooled and subdivided into a set of U—Pb analytical points based on their $^{238}U/^{208}Pb$ ratios in order to maximise ratio spread and produce an optimised isochron (Chew et al., 2021; Drost et al., 2018; Hoareau et al., 2021). However, caution needs to be taken when grouping pixels by their $^{238}U/^{208}Pb$ ratios as it can incorporate pixels from spatially distant regions of a sample and may remove the information about the spread of data that feeds into each analytical point. As such, we have

reported the U—Pb age results of both samples as a function of pixels pooled by their surrounding nearest neighbours in order to simulate pseudo-spot analysis (see Supplementary Material). Another approach that could be done is to group pixels by a geochemical proxy that is independent of the U—Pb isotopic system in order to establish a geochemical control on the spread of radiogenic Pb within a sample (Drost et al., 2018). A minimum of 30 pixels comprise one analytical point which approximately equates to an area of a ~ 100 μm spot size.

A secondary matrix-dependent fractionation correction done in Excel was then separately applied to the $^{238}U/^{206}Pb$ ratios of individual analytical points from the processed data based on the offset between the carbonate standard WC-1 age from the respective analytical session and its reported age (Drost et al., 2018; Roberts et al., 2017). The matrix-corrected (MC) ratios are then plotted as a mixing line between common Pb and radiogenic Pb in the Tera-Wasserburg space using IsoplotR, with the age of the sample interpreted as the lower Concordia intercept (Chew et al., 2014; Ludwig, 1998; Vermeesch, 2018). Reported uncertainties here are provided as 2SE and includes propagated reference material and decay constant uncertainties.

3.3.1. Imaging of laser raster pits

Systematic inaccuracies may result from differing matrix ablation characteristics between calibration materials and the samples analysed in this study (Guillong et al., 2020; Guillong and Günther, 2002). To investigate this potential issue, the ablated topography of laser raster pits of the samples and standards were imaged using an Olympus LEXT OLS5000 Profilometer at Adelaide Microscopy. These images have been used to assist in constraining the different ablation properties between the analysed 'dirty' dolostone unknowns, the NIST612 glass, the calcite neptunian dyke WC-1, and the lacustrine limestones Duff Tank and Mexican Tank.

4. Results

4.1. Mineralogy and petrography

High resolution BSE and MLA mapping of shale samples from the Amos Formation (Fig. 2) and the Balbirini Dolostone (Fig. 3) in this study indicate that samples BS20–02 and BS20–56 comprise of at least
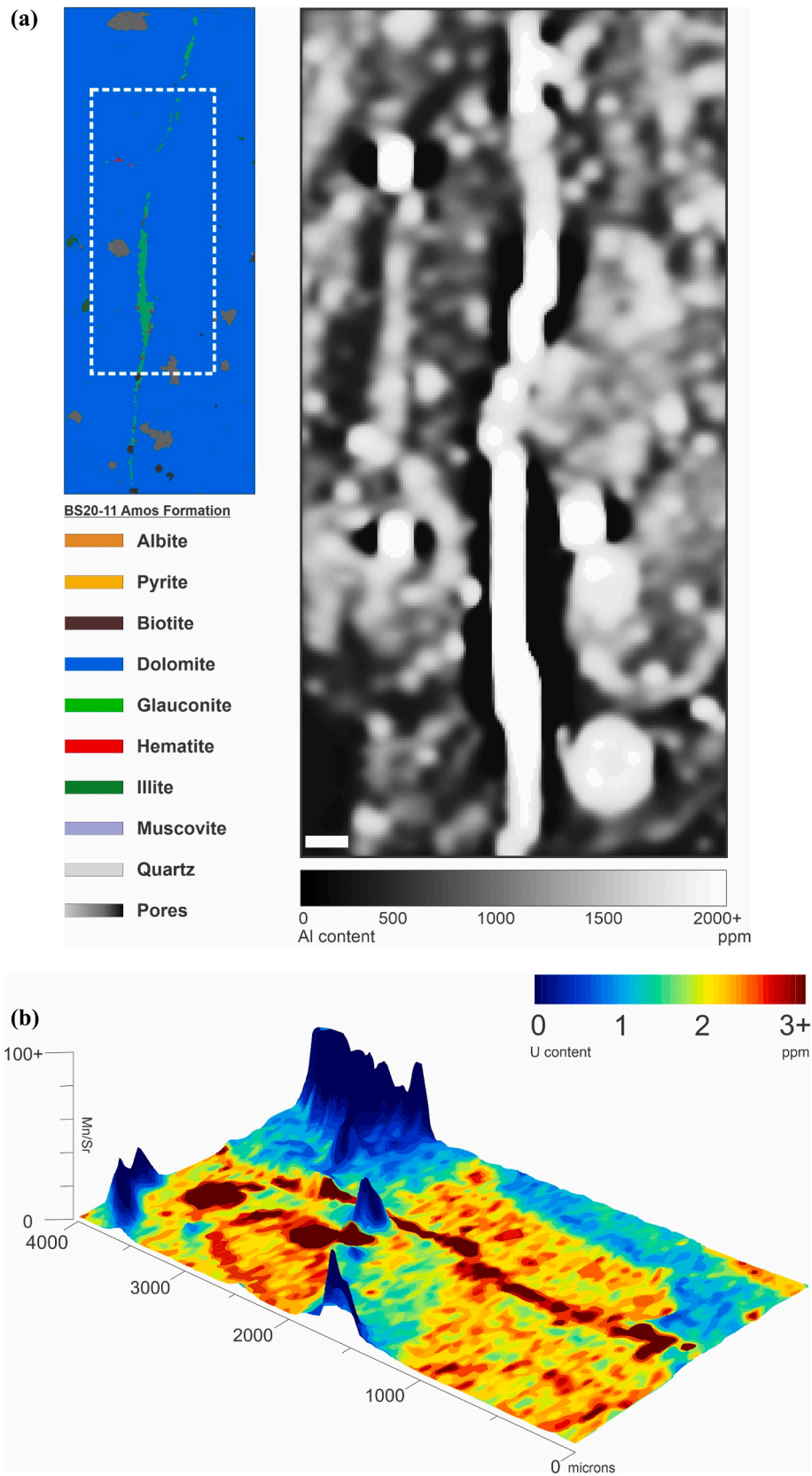
Fig. 4. A Mineralogy and petrography of dolostone sample BS20–11 from the Amos Formation. Non-carbonate phase can be observed in by MLA analysis and highlighted by elevated Al content. White bar = 100 μm. **4B.** Elevated Mn/Sr ratio here corresponds to low U content, suggesting that a post-depositional alteration event have removed Sr and U here. Note that the linear feature with elevated U corresponds to the bedding plane shown in Fig. 4A.
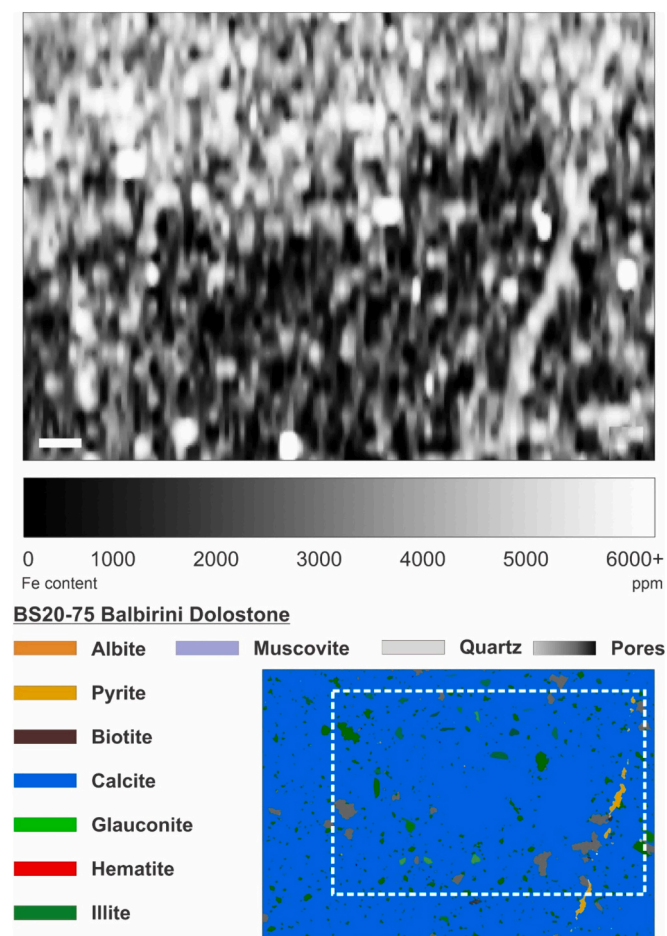
Fig. 5. Mineralogy and petrography of dolostone sample BS20–75 from the Balbirini Dolostone. Non-carbonate phases can be also observed in by MLA mapping of this sample. Another important feature is a pyrite vein cross-cutting the region, which corresponds to the elevated Fe content. White bar = 100 μm.

76.5% and 67.2% illite, respectively. Other K-rich aluminosilicate minerals identified in both samples include biotite, muscovite, and glauconite. However, these components make up a relatively minor component within BS20–02 (11.6%) and BS20–56 (12.1%). Other trace minerals identified in the shale samples include albite, calcite, hematite, quartz, rutile, and dolomite, which in total make up 11.9% in BS20–02 and 20.7% in BS20–56. The abundant clay minerals in both samples fill pore spaces or form a massive matrix in which larger detrital minerals are either cemented or 'float' within (Figs. 2 and 3). The orientations of illite and other clay minerals are random and do not follow a particular bedding plane. Particularly fine illite flakes concentrate in mottled domains, with individual grains difficult to distinguish. Additionally, these clays preserve their compaction features, wrapping around detrital quartz and albite (Figs. 2 and 3). Larger aluminosilicate minerals show evidence for transportation, showing textural maturity and appearing subangular with fragmented boundaries with grains aligned in a planar orientation. The illite components of samples BS20–02 and BS20–56 here are targeted for in-situ Rb—Sr geochronology.

The mineralogy of the dolostone samples comprise almost entirely of dolomite (BS20–11 = 94.8%, BS20–75 = 91.6%). Detrital minerals in BS20–11 (Fig. 4A) make up 5.2% and includes albite, quartz, rutile, illite, and montmorillonite. A non-carbonate phase can be observed following a bedding plane across a region of this sample. Similar detrital components are also found in BS20–75 (Fig. 5) and comprise 5.8% of the sample analysed. Notably, a pyrite vein can be observed cross-cutting the carbonate matrix in BS20–75 (Fig. 5). Regions including detrital

beds in BS20–11 and the sulphide vein in BS20–75 were targeted for laser ablation mapping in this study, to confirm the method's ability to be able to identify and discern the most pristine carbonate phase within mineralogically heterogeneous and partially altered sample. The total mineralogical make-up of each sample is provided in the Supplementary Information.

4.2. In-situ Rb—Sr geochronology

When anchored to an initial $^{86}Sr/^{87}Sr_i$ ratio of 1.3773 ± 0.0013 (Hogmalm et al., 2017), the phlogopite MDC analysed in the session resulted in an age of 534 ± 6 Ma (MSWD = 0.45, N = 20). Although this is ~2% older than the mean age of 519.4 ± 6.5 Ma for its nano-powder equivalent Mica-Mg (Govindaraju, 1979; Hogmalm et al., 2017), previous investigators have reported similar variability in age between pellet to pellet (Redaa et al., 2021; Redaa et al., 2023). The glauconite GL-O was dated 96 ± 4 Ma (MSWD = 0.81, N = 20), accurate to its mean age of 95.4 ± 4.6 Ma (Derkowski et al., 2009; Redaa et al., 2023).

Sample BS20–02 from the Amos Formation gave an age of 1604 ± 60 Ma (MSWD = 1.9, N = 50), while sample BS20–56 from the Balbirini Dolostone yielded a 1598 ± 34 Ma age (MSWD = 1.44 ± 0.04, N = 45). Their calculated $^{86}Sr/^{87}Sr_i$ ratio are 1.49 ± 0.09 and 1.44 ± 0.04, respectively. These values overlap with the expected $^{86}Sr/^{87}Sr$ signature of Proterozoic palaeoseawater ca. 1600 Ma at ~1.42 (Chen et al., 2022).

4.3. U—Pb geochronology and trace element mapping

U–Pb geochronology of calcite cement standard WC-1 gave an age of 229 ± 3 Ma when first corrected to glass reference material NIST612. This is younger than its reported age of 254.4 ± 6.4 Ma (Roberts et al., 2017). A secondary correction factor based on this variance is calculated and applied to the unknowns and secondary age checks in this study in order to account for the matrix difference between the glass and carbonate materials (Drost et al., 2018; Roberts et al., 2017; Roberts et al., 2020). The matrix corrected results of Duff Brown Tank defined an age of 59 ± 6 Ma (MSWD = 2.6, N = 11) while Mexican Tank was dated at 61 ± 4 Ma (MSWD = 3.1, N = 25). Hill et al. (2016) have noted that low proportions of secondary cements are present in both samples and may explain the dispersion in data from this study (i.e. MSWD >2). Nevertheless, these results are within uncertainty of their expected age of 64.04 ± 0.67 Ma (Duff Brown Tank) and 60.5 ± 4.6 Ma (Mexican Tank), respectively (Hill et al., 2016).

Data from Amos Formation sample BS20–11 were filtered to select the most pristine carbonate regions devoid of detrital input and diagenetic alteration by monitoring Ca and Al counts as well as Mn/Sr ratios. The area of the sample that successfully passed these criteria were 3483 pixels out of a possible 9275, and yielded an age of 1611 ± 19 Ma (Fig. 7, MSWD = 0.69, N = 99). Similarly, data from Balbirini Dolostone sample BS20–75 were also screened for detritus by monitoring Al counts. In addition, Fe and Y counts were also assessed to screen for the pyrite vein and possible hydrothermal alteration caused by it. Out of 12,261 possible pixels, 2974 met these criteria, and this was dated at 1608 ± 78 Ma (Fig. 7, MSWD = 1, N = 99).

4.3.1. Glass and carbonate laser ablation characteristics

Laser raster pits of glass standard NIST610 were approximately 12 μm deep (Fig. 6Ai–ii), while carbonates analysed in this study were consistently ablated deeper than 20 μm. In some cases such as the Mexican Tank carbonate, craters reached a depth of >30 μm (Fig. 6 Ci–ii). The bottom-crater profile of the NIST610 pit also differs in shape when compared to the carbonates. The glass left a relatively smooth, classical convex-shaped raster path while noisier craters were observed in the calcite standard WC-1 (Fig. 6Bi–ii). This is also seen in the limestone Duff Brown Tank and the Mexican Tank (Fig. 6ci–ii and 6di–ii, respectively), and dolostone samples BS20–11 (Fig. 6Ei–ii) and BS20–75 (Fig. 6Fi–ii). However, it should be noted that the ablation surfaces of

Table 2

Laser ablation and ICP-MS/MS operating parameters following Redaa et al. (2023); (Redaa et al., 2021).

Laser Parameters	Value	Unit
Ar carrier gas	880	ml/min
Fluence	3.5	J/cm^2
He carrier gas	380	ml/min
N$_2$ addition	3.5	ml/min
Repetition rate	5	Hz
Spot size	67	μm

ICP-MS/MS Plasma Parameters	Value	Unit
RF plasma power	1350	W

ICP-MS/MS Lens Parameters	Value	Unit
Lens extract 1	−2.0	V
Lens extract 2	−140	V
Omega bias	80	V
Omega lens	7	V
Q1 entrance	1.5	V
Q1 exit	−2	V
Cell focus	−2	V
Cell entrance	−90	V
Cell exit	−120	V
Deflect	−11	V
Plate bias	−80	V

ICP-MS/MS Q1 Parameters	Value	Unit
Q1 bias	−2	V
Q1 prefilter bias	−10	V
Q1 postfilter bias	−7	V

ICP-MS/MS Cell Parameters	Value	Unit
N2O flow rate	0.35	mL/min
OctP bias	−23	V
Axial acceleration	2	V
OctP RF	180	V
Energy discrimination	−8	V

ICP-MS/MS Q2 Parameters	Value	Unit
Q2 bias	−31	V

Elements analysed and dwell time parameters	Value	Unit
Na, Mg, Al, Si, P, K, Ca, Ti, Cr, Mn, Fe	2	ms
V, Cr, Cu, Y, Zr, Nb, Mo, La, Ce, Pr, Nd, Sm, Eu, Gd, Tb, Dy, Ho, Er, Tm, Yb, Lu, Th, U	5	ms
Rb	10	ms
^{88}Sr	20	ms
^{87}Sr, ^{86}Sr	50	ms

these carbonates were comparatively noisier with higher amplitude than WC-1. Nevertheless, similarity in ablation characteristics between the WC-1 standard and the other carbonates would suggest that WC-1 would be an appropriate matrix-match analogue for this study.

5. Discussion

5.1. In-situ Rb—Sr dating of authigenic clay minerals in shales

High resolution MLA mapping were conducted prior to the laser ablation analysis in order to categorise the mineralogy and petrography of all samples in this study (Fig. 2–5). For shales, the finest-grained,

homogeneous, black laminations were targeted to avoid obvious alteration overprints, veining, and incorporation of detrital minerals (Subarkah et al., 2022; Subarkah et al., 2023). Authigenic clay mineral assemblages were identified in both BS20–02 and BS20–56 and predominantly consist of illite, with minor glauconite present (Fig. 2–3). For BS20–02, these clays are commonly finer grained, filling pore spaces or forming a matrix or cement in which larger, detrital grains such as quartz are suspended in (Fig. 2). In BS20–56, sections of the sample contain illite flakes that are too fine to distinguish individually (Fig. 3). These mottled domains can wrap around detrital grains or preserve their initial compaction features. Such assemblages are interpreted to form in sediment, precipitating soon after deposition during the early diagenetic

Table 3
Laser ablation and ICP-MS operating parameters following Drost et al. (2018).

Laser	Value	Unit
He carrier gas	350	ml/min
Fluence	6–8	J/cm^2
Ar carrier gas	1	L/min
Scan speed	40	μm/s
Repetition rate	40	Hz
Spot size	80	μm square

Elements analysed and dwell time parameters	Value	Unit
Al, Si, P, Ca, Mn, Fe, Rb, Sr, Y, Zr, Ba, Ce	*2*	*ms*
Hg	*15*	*ms*
^{204}Pb	*20*	*ms*
^{206}Pb	*40*	*ms*
^{207}Pb	*50*	*ms*
^{208}Pb	*10*	*ms*
^{232}Th	*10*	*ms*
^{235}U	*20*	*ms*
^{238}U	*20*	*ms*

process (Deepak et al., 2022; Han et al., 2022; Rafiei, 2023; Rafiei et al., 2020; Rafiei et al., 2023; Rafiei and Kennedy, 2019; Subarkah et al., 2022). As such, they were targeted for in-situ Rb—Sr geochronology in order to determine their minimum depositional window.

Sample BS20–02 from the Amos Formation yielded an age of 1604 ± 60 Ma. This is within uncertainty of its depositional age of 1614 ± 4 Ma (Page et al., 2000), as constrained by tuffaceous zircons. Furthermore, sample BS20–56 sample from the Balbirini Dolostone was dated at 1598 ± 34 Ma, also consistent with the tuff ages from the unit aged 1613 ± 4 Ma and 1609 ± 3 Ma (Page et al., 2000). Notably, the Rb—Sr age of BS20–56 is also in agreement with the maximum depositional ages of the section dated by detrital zircons at 1625 ± 14 Ma and 1607 ± 6 Ma (Kositcin and Munson, 2020). Consequently, the Rb—Sr ages are interpreted to record the depositional age of the Amos Formation and the Balbirini Dolostone (Fig. 1). This is further corroborated by the petrographic evidence of each sample (Fig. 2–3), as the illite morphology targeted for laser ablation suggest that they are authigenic or early diagenetic in nature (Deepak et al., 2022; Han et al., 2022; Rafiei, 2023; Rafiei et al., 2020; Rafiei et al., 2023; Rafiei and Kennedy, 2019; Subarkah et al., 2022). In addition, the calculated initial ^{86}Sr/^{87}Sr composition of the samples analysed also overlap with the estimated palaeoseawater ^{86}Sr/^{87}Sr ratios ca. 1600 Ma (Chen et al., 2022). These observations indicate that the ablated minerals precipitated out of the coeval water-column and hence record a primary seawater isotopic signature, as opposed to reflecting detrital or later-stage alteration signatures.

It should be noted that the difference of precision between the two samples can be attributed to the spread in ^{87}Rb/^{87}Sr ratios and uncertainty associated with each individual analysis (Nebel, 2014). Sample BS20–56 has a spread of ^{87}Rb/^{87}Sr ratios between 5 and 30 and yielded a 2SE precision of 2.1%. On the other hand, BS20–02 had a relatively limited spread in ^{87}Rb/^{87}Sr ratios of 22–32 and resulted in 3.7% precision. Nevertheless, the accuracy of the shale in-situ Rb—Sr geochronology results here in relation to their expected depositional ages further shows that the use of Mica-Mg nano-powder as a primary reference material for dating fine-grained clays does not induce any significant matrix-related age offsets.

5.2. Image mapping approach for U—Pb geochronology and geochemistry of carbonates

The difference in matrix and related ablation properties between the unknowns and the standards used during an analytical session will cause an offset on the resulting calculated carbonate U—Pb geochronology (Rasbury et al., 2021; Roberts et al., 2017). This is accounted for by a

correction factor applied to the unknowns that depends on the offset between the published age of the Reference Material used (in this case, WC-1) and its observed age in the corresponding analytical session (Roberts et al., 2017). Ablation pit craters from the standards and unknowns in this study were mapped (Fig. 6) in order to assess the varying characteristics between the glass standard NIST612, calcite WC-1, lacustrine limestone Duff Brown Tank and Mexican Tank, and the dolostone samples BS20–11 and BS20–75. The raster pits of glass standard NIST612 (Fig. 6Ai–ii) were convex, more stable, and around 50% shallower than those observed in the carbonates from this study. On the other hand, all of the craters in both the carbonate standards and unknowns were ablated to between 20 and 30 μm deep, likely a consequence of their similar mineralogy. Their bottom-hole raster craters are also noisier in comparison to the NIST612 glass. However, WC-1, Duff Brown Tank, and the Mexican Tank all display less variability in amplitude of noise when compared to the craters in BS20–11 and BS20–75 (Fig. 6). Such dissimilarities likely reflect the difference in matrix related ablation properties between calcite and dolomite. However, the correction factor based on WC-1 appears viable for both minerals and yield data consistent with previous age constraints of the respective dated samples, as would be expected for minerals which exhibit no clear characteristics of post-depositional alteration or overprint (Fig. 7). Consequently, we suggest that despite not being a perfect match, it is still appropriate to normalise dolomite samples to WC-1. We also note that this matrix difference may also result in session-to-session variability of results from Duff Brown Tank and Mexican Tank, as they may not be as crystalline and homogeneous in comparison to WC-1. Nevertheless, it is important to develop a dolomite standard for U—Pb geochronology in order to reduce the uncertainties of the dated material (Elisha et al., 2021). Furthermore, the precision in the age data can also be improved by a better spread in radiogenic Pb, as well as smaller uncertainties on the individual data points (Jahn et al., 1990; Rasbury and Cole, 2009). For the image mapping approach, this can be a factor of how many pixels pass the selection criteria and then pooled for U—Pb geochronology; as uncertainties on individual points can be reduced by incorporating more pixels into them (Drost et al., 2018; Hoareau et al., 2021; Kim et al., 2023; Roberts et al., 2020). Drost et al. (2018) have noted that this is also particularly beneficial for young (Cenozoic) samples or those with low U concentration (<0.5 ppm). The advantage of increasing the numbers of pixels pooled into an analysis observed in this study, as each analytical point in BS20–11 contain 40 pixels and gave uncertainties of 1.2% while BS20–75 had 30 pixels for every data point and yielded age uncertainties of 4.8%. Notably, this difference occurs despite the samples having a similar spread in ^{238}U/^{206}Pb ratios (Fig. 7).

Laser ablation mapping of the sample BS20–11 from the Amos Formation was able to identify the non-carbonate bedding in the sample by monitoring Al content (Fig. 4A). As such, low Al and high Ca were added as the filtering criteria in order to avoid mixed signals from different mineral assemblages (Drost et al., 2018). In addition, the Mn/Sr ratio of the sample (Fig. 4B) was also highlighted to assess post-depositional alteration (Banner and Hanson, 1990; Brand and Veizer, 1980; Jacobsen and Kaufman, 1999; Kaufman and Knoll, 1995). Diagenetic processes can cause an enrichment of Mn and depletion of Sr in carbonates. Consequently, carbonates that have experienced extensive alteration are likely to have higher Mn/Sr ratios (Banner and Hanson, 1990; Brand and Veizer, 1980; Jacobsen and Kaufman, 1999; Kaufman and Knoll, 1995). Notably, regions in BS20–11 with high Mn/Sr ratios correspond to lower U content, suggesting that alteration mobilised both Sr and U in the sample (Fig. 4B). Therefore, areas with high Mn/Sr and low U are filtered out from further investigations to exclude regions of post diagenetic alteration. The pixels of the remaining unaltered carbonate were subdivided by their ^{238}U/^{208}Pb ratios and yielded an age of 1611 ± 19 Ma. This agrees with previous estimates for the time of deposition (Kositcin and Munson, 2020; Munson, 2019; Page et al., 2000), as well as the in-situ Rb—Sr dating of a shale sample 22 m below this carbonate
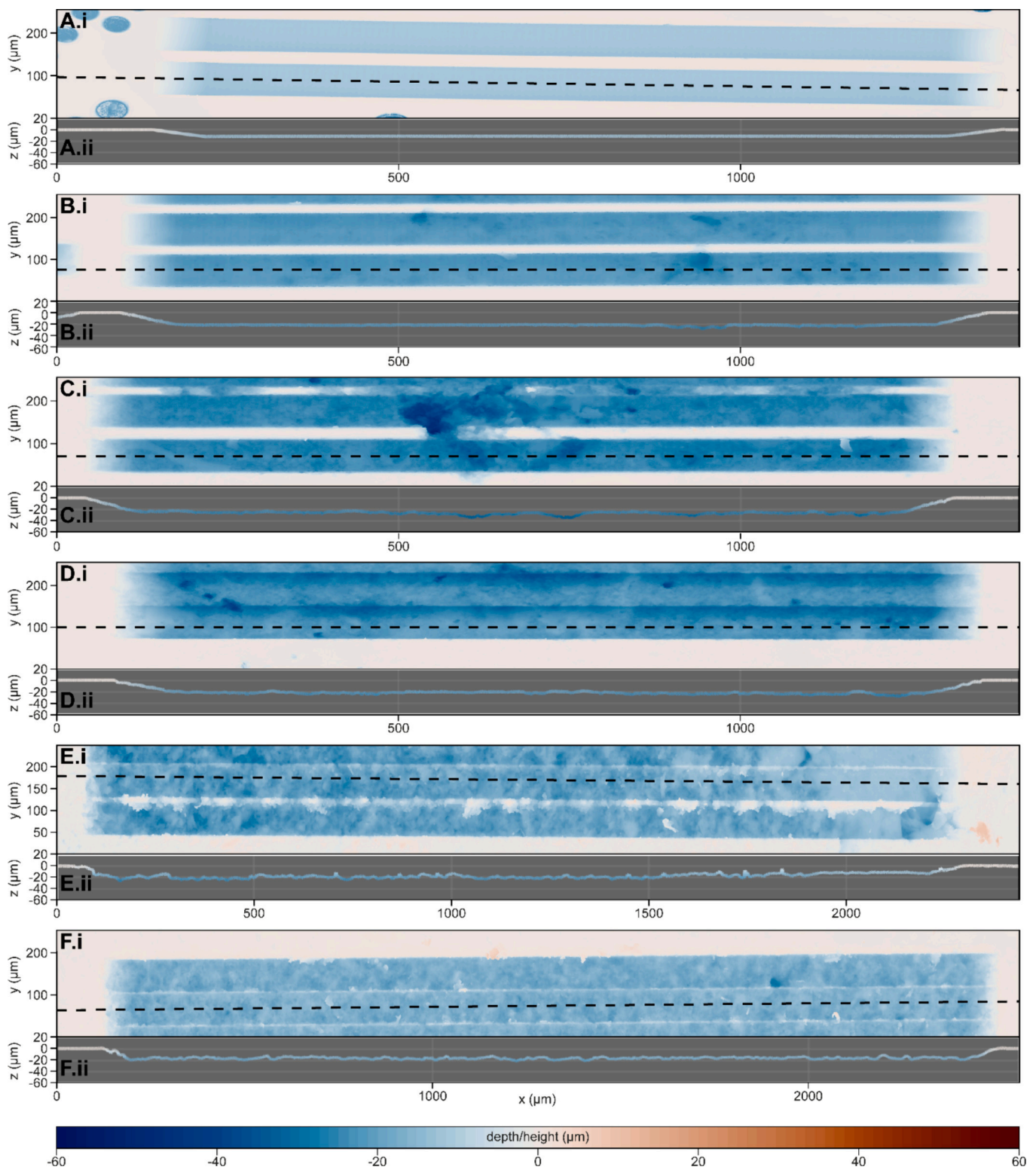
Fig. 6. Mapping of raster craters of NIST612 (6 A), WC-1 (6B), Mexican Tank (6C), Duff Brown Tank (6D), BS20–11 (6E), and BS20–75 (6F). Images shown in the ii sections are the respective down-hole craters of raster trajectories shown by the black dashed lines. (For interpretation of the references to colour in this figure legend, the reader is referred to the web version of this article.)

sample (Fig. 1). In addition, the same pixels which have passed the selection criteria were also grouped by their gridded nearest neighbour in order to replicate pseudo-spot analyses and gave a U—Pb age of 1614 ± 30 Ma (Supplementary Information). This approach was taken in order to verify the validity of splitting the pixels by their $^{238}U/^{208}Pb$ ratios, as it can remove the spatial context of the data despite inherently

generating an isochron with good statistical fit. Both approaches gave ages within uncertainties of each other and consequently, the most pristine carbonate regions of BS20–11 are interpreted to record the depositional age of the Amos Formation.

Elevated Fe in sample BS20–75 (Fig. 5) from the Balbirini Dolostone was used to isolate the pyrite vein identified by prior BSE and MLA
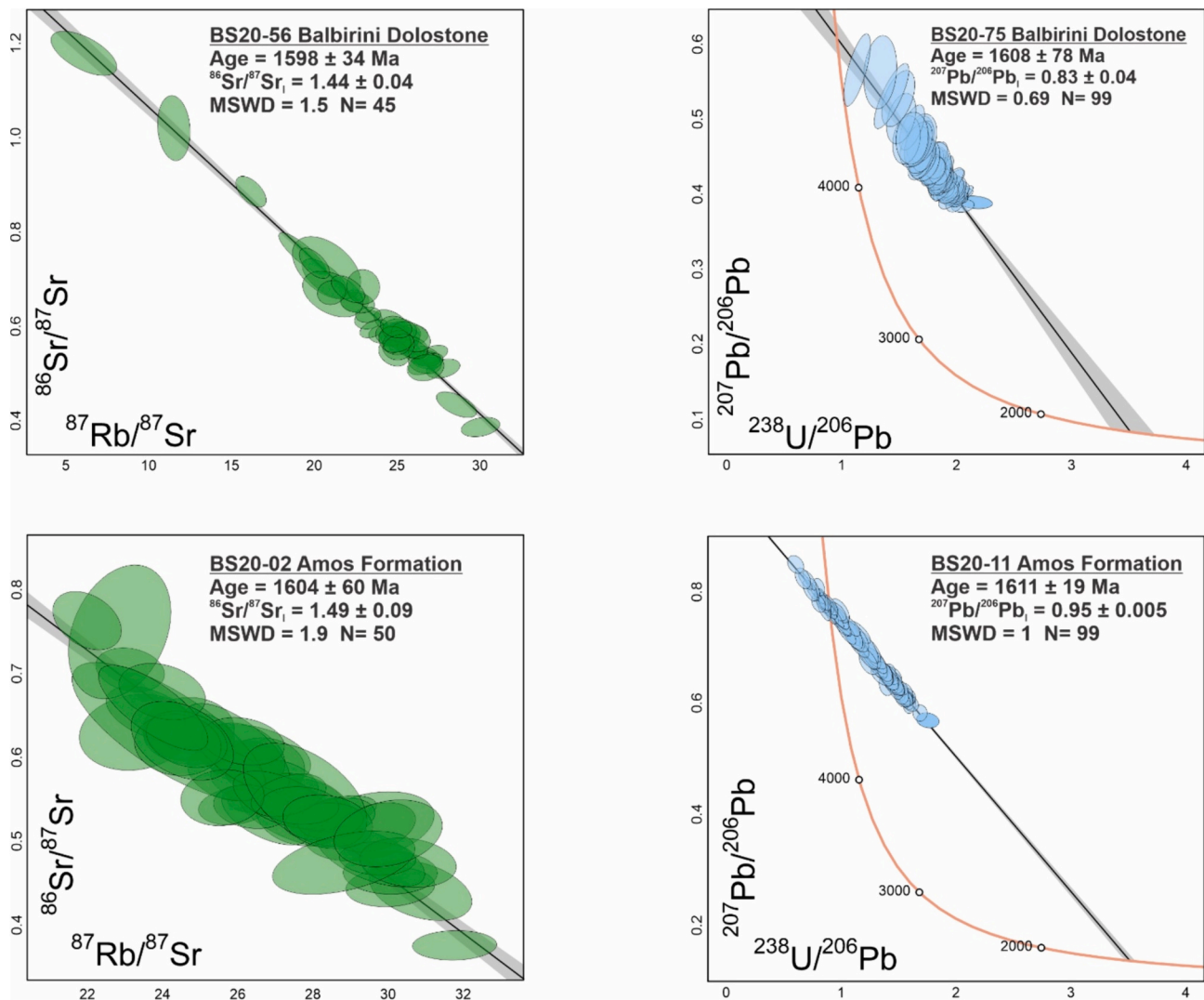
Fig. 7. Summary of geochronological results in this study. Note that samples with a better spread in radiogenic isotopic ratios and smaller uncertainties in each analytical point will result in an improved age uncertainty in both dating techniques.

mapping. Furthermore, yttrium values were also monitored to assess possible mobilisation of rare earth and trace elements related to hydrothermal input as they commonly fractionate in hydrothermal systems (Bau et al., 1997; Bau and Dulski, 1995; Bau and Dulski, 1996). Lastly, elevated Al values of this sample were also applied as a filter criterion to minimise the effects of detrital input. The filtered, pristine, carbonate yielded a U—Pb age of 1608 ± 78 Ma, accurate to the previous age constraints of the Balbirini Dolostone by SIMS U—Pb dating of tuffs (Page et al., 2000), detrital zircons (Kositcin and Munson, 2020), and in-situ Rb—Sr geochronology of authigenic illite in shales from this study, which is 64 m stratigraphically below this sample (Fig. 1). In addition, the carbonate phase in this sample was also grouped by their gridded nearest neighbour pixels and gave an age within uncertainties of the aforementioned geochronology constraints as well (1642 ± 97 Ma, Supplementary Material). As a result, BS20–75 also appears to retain the depositional history of its corresponding unit.

This study demonstrates that the laser image mapping approach was able to effectively isolate the most pristine carbonate phase of a sample through its petrography and geochemistry. In addition, discrete heterogeneity within carbonate phases which may not be identified just through mineral mapping can be highlighted by major and trace element proxies. Furthermore, this approach benefits from the ability to pool the cogenetic regions based on their U concentration and radiogenic

isotopes. This improves the likelihood of capturing sufficient spread required for robust isochron construction, an issue commonly associated with spot ablation U—Pb dating of carbonates (Roberts et al., 2020).

6. Conclusions

In this case study we demonstrate that Rb—Sr and U—Pb techniques are able to confidently constrain the primary depositional chronology of lithologically diverse and complex Proterozoic sedimentary successions. This is made possible by combining the petrographic, geochemical, and geochronological data of a sample. Input from non-cogenetic phases such as detrital or alteration minerals can be spatially avoided or filtered through monitoring particular geochemical proxies. Consequently, sedimentary units that are devoid of tuff beds or biostratigraphic correlations may now be directly constrained through these avenues, with multi-method chronology providing independent validation through complementary isotopic systems. Potential sedimentary sequences to be resolved through this approach include geologically significant successions such as stratigraphy exhibiting global geochemical excursions, synchronous cap carbonates, or sediment-hosted mineral deposits.

Case study samples from the Proterozoic Amos Formation and the Balbirini Dolostone in the McArthur Basin were dated within 1–5% precision. This precision discrepancy is dominantly controlled by the

spread in radiogenic ratios and the magnitude of individual uncertainties on each analytical point (Drost et al., 2018; Hoareau et al., 2021; Kim et al., 2023; Nebel, 2014; Roberts et al., 2020). For dolomite U—Pb geochronology, this can likely be improved by developing a matrix-matched standard. Nonetheless, results from in-situ shale Rb—Sr geochronology and U—Pb carbonate laser mapping are consistent with their depositional ages as constrained by dating of tuff beds and detrital zircons sourced from the same locality of the unknown samples, demonstrating the applicability of this combined methodology to sedimentary carbonates devoid of such traditional chronological markers such as tuff sequences or biostratigraphy. (Kositcin and Munson, 2020; Munson, 2019; Page et al., 2000).

CRediT authorship contribution statement

Darwinaji Subarkah: Writing – review & editing, Writing – original draft, Visualization, Software, Methodology, Investigation, Formal analysis, Data curation, Conceptualization. **Angus L. Nixon:** Writing – review & editing, Methodology, Data curation. **Sarah E. Gilbert:** Writing – review & editing, Methodology, Data curation, Conceptualization. **Alan S. Collins:** Writing – review & editing, Validation, Supervision, Resources, Project administration, Investigation, Funding acquisition. **Morgan L. Blades:** Writing – review & editing, Validation, Supervision, Project administration. **Alexander Simpson:** Writing – review & editing, Formal analysis, Data curation, Conceptualization. **Jarred C. Lloyd:** Writing – review & editing, Methodology, Data curation. **Georgina M. Virgo:** Conceptualization, Data curation, Investigation, Methodology, Project administration. **Juraj Farkaš:** Writing – review & editing, Supervision, Funding acquisition.

Declaration of competing interest

The authors declare the following financial interests/personal relationships which may be considered as potential competing interests. No competing interests to declare.

Acknowledgements

Appendix A. Supplementary data

Supplementary data to this article can be found online at https://doi.org/10.1016/j.lithos.2024.107649.

References

Ahmad, A., Munson, T.J., 2013. Geology and mineral resources of the Northern Territory. In: Special Publication, 5. Northern Territory Geological Survey.

Banner, J., Hanson, G., 1990. Calculation of simultaneous isotopic and trace element variations during water-rock interaction with applications to carbonate diagenesis. Geochim. Cosmochim. Acta 54, 3123–3137.

Bau, M., Dulski, P., 1995. Comparative study of yttrium and rare-earth element behaviours in fluorine-rich hydrothermal fluids. Contrib. Mineral. Petrol. 119 (2), 213–223.

Bau, M., Dulski, P., 1996. Distribution of yttrium and rare-earth elements in the Penge and Kuruman iron-formations, Transvaal Supergroup, South Africa. Precambrian Res. 79 (1–2), 37–55.

Bau, M., Möller, P., Dulski, P., 1997. Yttrium and lanthanides in eastern Mediterranean seawater and their fractionation during redox-cycling. Mar. Chem. 56 (1–2), 123–131.

Brand, U., Veizer, J., 1980. Chemical diagenesis of a multicomponent carbonate system; 1, Trace elements. J. Sediment. Res. 50 (4), 1219–1236.

Chen, X., Zhou, Y., Shields, G.A., 2022. Progress towards an improved Precambrian seawater 87Sr/86Sr curve. Earth Sci. Rev. 224, 103869.

Chew, D.M., Petrus, J.A., Kamber, B.S., 2014. U–Pb LA–ICPMS dating using accessory mineral standards with variable common Pb. Chem. Geol. 363, 185–199.

Chew, D., Drost, K., Marsh, J.H., Petrus, J.A., 2021. LA-ICP-MS imaging in the geosciences and its applications to geochronology. Chem. Geol. 559, 119917.

Close, D., 2014. The McArthur Basin: NTGS' Approach to a Frontier Petroleum Basin with Known Base Metal Prospectivity. Annual Geoscience Exploration Seminar Northern Territory Geological Survey, Alice Springs.

Collins, A., et al., 2019. Life and Times of the Proterozoic McArthur-Yanliao Gulf: Update on the ARC-Industry-NTGS Linkage Project. Alice Springs, Northern Territory, Australia, pp. 44–48. https://geoscience.nt.gov.au/gemis/ntgsjspui/handle/1/88374.

Cox, G.M., et al., 2022. A very unconventional hydrocarbon play: the Mesoproterozoic Velkerri Formation of northern Australia. AAPG Bull. 106 (6), 1213–1237.

Deepak, A., et al., 2022. Testing the Precambrian reverse weathering hypothesis using a 1-billion-year record of marine shales. In: Goldschmidt Conference. Goldschmidt.

Derkowski, A., et al., 2009. Partial dissolution of glauconitic samples: Implications for the methodology of K-Ar and Rb-Sr dating. Clay Clay Miner. 57 (5), 531–554.

Drake, H., Tillberg, M., Reinhardt, M., Whitehouse, M.J., Kooijman, E., 2023. In Situ Rb/Sr Geochronology and Stable Isotope Geochemistry evidence for Neoproterozoic and Paleozoic Fracture-Hosted Fluid Flow and Microbial activity in Paleoproterozoic Basement, SW Sweden. Geochem. Geophys. Geosyst. 24 (5) e2023GC010892.

Drost, K., et al., 2018. An image Mapping Approach to U-Pb LA-ICP-MS Carbonate Dating and applications to Direct Dating of Carbonate Sedimentation. Geochem. Geophys. Geosyst. 19 (12), 4631–4648.

Elisha, B., Nuriel, P., Kylander-Clark, A., Weinberger, R., 2021. Towards in situ U–Pb dating of dolomite. Geochronology 3 (1), 337–349.

Govindaraju, K., 1979. Report (1968–1978) on two Mica Reference Samples: Biotite Mica-Fe and Phlogopite Mica-Mg. Geostand. Newslett. 3 (1), 3–24.

Gradstein, F.M., 2012. Chapter 3 - Biochronology. In: Gradstein, F.M., Ogg, J.G., Schmitz, M.D., Ogg, G.M. (Eds.), The Geologic Time Scale. Elsevier, Boston, pp. 43–61.

Guillong, M., Günther, D., 2002. Effect of particle size distribution on ICP-induced elemental fractionation in laser ablation-inductively coupled plasma-mass spectrometry. J. Anal. At. Spectrom. 17 (8), 831–837.

Guillong, M., Wotzlaw, J.-F., Looser, N., Laurent, O., 2020. Evaluating the reliability of U–Pb laser ablation inductively coupled plasma mass spectrometry (LA-ICP-MS) carbonate geochronology: matrix issues and a potential calcite validation reference material. Geochronology 2 (1), 155–167.

Han, S., et al., 2022. Earth system science applications of next-generation SEM-EDS automated mineral mapping. Front. Earth Sci. 10.

Hestnes, Å., et al., 2023. Constraining the tectonic evolution of rifted continental margins by U–Pb calcite dating. Sci. Rep. 13 (1), 7876.

Hill, C.A., Polyak, V.J., Asmerom, Y., Provencio, P., 2016. Constraints on a late cretaceous uplift, denudation, and incision of the Grand Canyon region, southwestern Colorado Plateau, USA, from U-Pb dating of lacustrine limestone. Tectonics 35 (4), 896–906.

Hoareau, G., et al., 2021. Direct U–Pb dating of carbonates from micron-scale femtosecond laser ablation inductively coupled plasma mass spectrometry images using robust regression. Geochronology 3 (1), 67–87.

Hogmalm, K.J., Zack, T., Karlsson, A.K.O., Sjöqvist, A.S.L., Garbe-Schönberg, D., 2017. In situ Rb–Sr and K–Ca dating by LA-ICP-MS/MS: an evaluation of N2O and SF6 as reaction gases. J. Anal. At. Spectrom. 32 (2), 305–313.

Holland, H.D., 2006. The oxygenation of the atmosphere and oceans. Philos. Trans. R. Soc. B 361 (1470), 903–915.

Hunt, J.M., 1995. Petroleum Geochemistry and Geology.

Jackson, M.J., Muir, M.D., Plumb, K.A., 1987. Geology of the Southern McArthur Basin, Northern Territory. Australian Government Public Service.

Jacobsen, S.B., Kaufman, A.J., 1999. The Sr, C and O isotopic evolution of Neoproterozoic seawater. Chem. Geol. 161 (1), 37–57.

Jahn, B.-M., Bertrand-Sarfati, J., Morin, N., Macé, J., 1990. Direct dating of stromatolitic carbonates from the Schmidtsdrif Formation (Transvaal Dolomite), South Africa, with implications on the age of the Ventersdorp Supergroup. Geology 18 (12), 1211–1214.

Jochum, K.P., et al., 2011. Determination of Reference Values for NIST SRM 610–617 Glasses following ISO guidelines. Geostand. Geoanal. Res. 35 (4), 397–429.

Kaufman, A.J., Knoll, A.H., 1995. Neoproterozoic variations in the C-isotopic composition of seawater: stratigraphic and biogeochemical implications. Precambrian Res. 73 (1–4), 27–49.

Kim, H., et al., 2023. Principle and Application of 'Image-mapping'in-situ U-Pb Carbonate Age-dating. Econom. Enviro. Geol. 56 (2), 115–123.

Kositcin, N., Munson, T.J., 2020. Summary of Results. Joint NTGS-GA Geochronology Project: Balbirini Dolostone, Southern McArthur Basin, June 2019–September 2019. 2020–002. Northern Territory Geological Survey, Northern Territory, Australia.

Lan, Z., et al., 2024. Black shale LA-ICP-MS Rb-Sr and monazite SIMS U-Pb geochronology from the Cryogenian successions in the northern Yangtze Block. Precambrian Res. 401, 107277.

Laureijs, C.T., Coogan, L.A., Spence, J., 2021. In situ Rb-Sr dating of celadonite from altered upper oceanic crust using laser ablation ICP-MS/MS. Chem. Geol. 120339.

Levorsen, A.I., Berry, F.A., 1967. Geology of Petroleum. WH Freeman San Francisco.

Li, Y., Vermeesch, P., 2021. Short communication: Inverse isochron regression for Re–Os, K–Ca and other chronometers. Geochronology 3 (2), 415–420.

Li, Q., Parrish, R.R., Horstwood, M.S.A., McArthur, J.M., 2014. U–Pb dating of cements in Mesozoic ammonites. Chem. Geol. 376, 76–83.

Lloyd, J.C., et al., 2023. Geochronology and formal stratigraphy of the Sturtian Glaciation in the Adelaide Superbasin. Geol. Mag. 160 (7), 1321–1344.

Ludwig, K.R., 1998. On the Treatment of Concordant Uranium-Lead Ages. Geochim. Cosmochim. Acta 62 (4), 665–676.

Lyons, T.W., Gellatly, A.M., McGoldrick, P.J., Kah, L.C., 2006. Proterozoic sedimentary exhalative (SEDEX) deposits and links to evolving global ocean chemistry. Memoirs-Geol. Soc. America 198, 169.

Lyons, T.W., Reinhard, C.T., Planavsky, N.J., 2014. The rise of oxygen in Earth's early ocean and atmosphere. Nature 506 (7488), 307–315.

Lyons, T.W., Diamond, C.W., Planavsky, N.J., Reinhard, C.T., Li, C., 2021. Oxygenation, Life, and the Planetary System during Earth's Middle history: an Overview. Astrobiology 21 (8), 906–923.

McDougall, I., 2013. Volcanic Rocks (K–Ar and Ar–Ar). In: Rink, W.J., Thompson, J. (Eds.), Encyclopedia of Scientific Dating Methods. Springer, Netherlands, Dordrecht, pp. 1–8.

Monchal, V., Drost, K., Chew, D., 2023. Precise U-Pb dating of incremental calcite slickenfiber growth: evidence for far-field Eocene fold reactivation in Ireland. Geology 51 (7), 611–615.

Mukherjee, I., Large, R.R., 2020. Co-evolution of trace elements and life in Precambrian oceans: the pyrite edition. Geology 48 (10), 1018–1022.

Munson, T., 2019. Detrital Zircon Geochronology Investigations of the Glyde and Favenc Packages: Implications for the Geological Framework of the Greater McArthur Basin, Northern Territory: In Annual Geoscience Exploration Seminar (AGES) Proceedings, Alice Springs, Northern Territory, 19–20 March 2019. Northern Territory Geological Survey, Darwin.

Nebel, O., 2014. Rb–Sr Dating, Encyclopedia of Scientific Dating. Methods 1–19.

Nicolaysen, L.O., 1961. Graphic Interpretation of Discordant Age Measurements on Metamorphic Rocks. Ann. N. Y. Acad. Sci. 91 (2), 198–206.

Page, R., Jackson, M., Krassay, A., 2000. Constraining sequence stratigraphy in north Australian basins: SHRIMP U–Pb zircon geochronology between Mt Isa and McArthur River. Aust. J. Earth Sci. 47 (3), 431–459.

Paton, C., Hellstrom, J., Paul, B., Woodhead, J., Hergt, J., 2011. Iolite: Freeware for the visualisation and processing of mass spectrometric data. J. Anal. At. Spectrom. 26 (12), 2508–2518.

Petrus, J.A., Chew, D.M., Leybourne, M.I., Kamber, B.S., 2017. A new approach to laser-ablation inductively-coupled-plasma mass-spectrometry (LA-ICP-MS) using the flexible map interrogation tool 'Monocle'. Chem. Geol. 463, 76–93.

Pietsch, B., 1991. 1: 2500000 Geological Map Series and Explanatory Notes SE 53–03. Northern Territory Geological Survey.

Rafiei, M., 2023. Petrographic and Geochemical Screening of Clay Genesis for Paleoweathering and Geochronology Applications. Macquarie University.

Rafiei, M., Kennedy, M., 2019. Weathering in a world without terrestrial life recorded in the Mesoproterozoic Velkerri Formation. Nat. Commun. 10 (1), 3448.

Rafiei, M., Löhr, S., Baldermann, A., Webster, R., Kong, C., 2020. Quantitative petrographic differentiation of detrital vs diagenetic clay minerals in marine sedimentary sequences: Implications for the rise of biotic soils. Precambrian Res. 350, 105948.

Rafiei, M., et al., 2023. Microscale Petrographic, Trace Element, and Isotopic Constraints on Glauconite Diagenesis in Altered Sedimentary Sequences: Implications for Glauconite Geochronology. Geochem. Geophys. Geosyst. 24 (4) e2022GC010795.

Rasbury, E.T., Cole, J.M., 2009. Directly dating geologic events: U-Pb dating of carbonates. Rev. Geophys. 47 (3).

Rasbury, E.T., et al., 2021. Tools for uranium characterization in carbonate samples: case studies of natural U–Pb geochronology reference materials. Geochronology 3 (1), 103–122.

Redaa, A., Farkaš, J., Gilbert, S., Collins, A.S., Wade, B., Löhr, S., Zack, T., Garbe-Schönberg, D., 2021. Assessment of elemental fractionation and matrix effects during in situ Rb–Sr dating of phlogopite by LA-ICP-MS/MS: implications for the accuracy and precision of mineral ages. J. Anal. At. Spectrom. 36 (2), 322–344. https://doi.org/10.1039/d0ja00299b.

Redaa, A., et al., 2023. Testing Nano-Powder and Fused-Glass Mineral Reference Materials for in Situ Rb-Sr Dating of Glauconite, Phlogopite, Biotite and Feldspar via LA-ICP-MS/MS. Geostand. Geoanal. Res. 47 (1), 23–48.

Rimstidt, J.D., Balog, A., Webb, J., 1998. Distribution of trace elements between carbonate minerals and aqueous solutions. Geochim. Cosmochim. Acta 62 (11), 1851–1863.

Roberts, N.M.W., Holdsworth, R.E., 2022. Timescales of faulting through calcite geochronology: a review. J. Struct. Geol. 158, 104578.

Roberts, N.M.W., et al., 2017. A calcite reference material for LA-ICP-MS U-Pb geochronology. Geochem. Geophys. Geosyst. 18 (7), 2807–2814.

Roberts, N.M.W., et al., 2020. Laser ablation inductively coupled plasma mass spectrometry (LA-ICP-MS) U–Pb carbonate geochronology: strategies, progress, and limitations. Geochronology 2 (1), 33–61.

Roberts, N.M.W., Žák, J., Vacek, F., Sláma, J., 2021. No more blind dates with calcite: Fluid-flow vs. fault-slip along the Očkov thrust, Prague Basin. Geosci. Front. 12 (4), 101143.

Rösel, D., Köhler, M., Petts, A., Zack, T., 2023. In-Situ Rb-Sr Dating of Detrital mica and its Application for Provenance Studies. Copernicus Meetings.

Scheiblhofer, E., et al., 2022. Revisiting Glauconite Geochronology: Lessons Learned from in Situ Radiometric Dating of a Glauconite-Rich Cretaceous Shelfal Sequence, Minerals.

Sippel, R.F., Glover, E.D., 1964. The solution alteration of carbonate rocks, the effects of temperature and pressure. Geochim. Cosmochim. Acta 28 (9), 1401–1417.

Spandler, C., Slezak, P., Nazari-Dehkordi, T., 2020. Tectonic significance of Australian rare earth element deposits. Earth Sci. Rev. 207, 103219.

Subarkah, D., et al., 2022. Constraining the geothermal parameters of in situ Rb–Sr dating on Proterozoic shales and their subsequent applications. Geochronology 4 (2), 577–600.

Subarkah, D., et al., 2023. Characterising the economic Proterozoic Glyde Package of the greater McArthur Basin, northern Australia. Ore Geol. Rev. 158, 105499.

Subarkah, D., Blades, M.L., Collins, A.S., Farkaš, J., Gilbert, S., Löhr, S.C., Redaa, A., Cassidy, E., Zack, T., 2022. Unraveling the histories of Proterozoic shales through in situ Rb-Sr dating and trace element laser ablation analysis. Geology 50 (1), 66–70. https://doi.org/10.1130/G49187.1.

Vermeesch, P., 2018. IsoplotR : a free and open toolbox for geochronology. Geosci. Front. 9.

Wu, Y., Bai, X.-J., Shi, H.-S., He, L.-Y., Qiu, H.-N., 2023. Dating of authigenic minerals in sedimentary rocks: a review. Earth Sci. Rev. 241, 104443.

Zack, T., Hogmalm, K.J., 2016. Laser ablation Rb/Sr dating by online chemical separation of Rb and Sr in an oxygen-filled reaction cell. Chem. Geol. 437, 120–133.